Corrosion of carbon steel in clay compact environments at 90 °C: Effect of confined conditions

M.L. Schlegel, F. Martin, M. Fenart, C. Blanc, J. Varlet, E. Foy

Corrosion of carbon steel in clay compact environments at 90 °C: effect of confined conditions

M. L. Schlegel[1], F. Martin[2], M. Fenart[2], C. Blanc[1], J. Varlet[1], E. Foy[3]

1 Université Paris Saclay, CEA, Service d'Études Analytiques et de Réactivité des Surfaces, 91191, Gif-sur-Yvette, France.

2 Université Paris Saclay, CEA, Service de Corrosion et du Comportement des Matériaux dans leurs Environnements, 91191, Gif-sur-Yvette, France

3 LAPA-IRAMAT, NIMBE, CEA, CNRS, Université Paris Saclay, CEA Saclay, F-91191 Gif-sur-Yvette, France

Abstract

Corrosion of low alloy carbon steel in simulated crevices and in a perforated envelope containing a rod, mimicking the liner-overpack system, was assessed at 90 °C in anoxic water-saturated clay. Corrosion in crevices was limited (< 1 µm/year). The corroded surface exposed magnetite with a fringe of siderite. Internal corrosion of the envelope was heterogeneous due to gradual filling with porewater, and average corrosion depth for the internal rod was limited to 11.5 µm after 76 months. Magnetite was the main corrosion product replacing steel, together with chukanovite, Fe silicate, and outer siderite in areas first bathed with porewater.

Keywords

Carbon steel (A) ; Clay (A); SEM (B) ; XRD (B) ; Raman spectroscopy (B)

1 Introduction

Decades of investigation on the management of high-level radioactive waste (HLW) established disposal in geologic repositories as the safest and most sustainable approach to deal with this legacy of nuclear industry [1-3]. In these disposal facilities, confinement of HLW is imparted to metallic canisters embedded in bentonite, clay, or concrete barriers [4, 5]. For example, the early French project for a deep underground disposal [6] relied on encapsulation of nuclear glass in stainless steel containers and low-alloy steel (C-steel) overpacks inserted in steel-lined boreholes within the Callovo-Oxfordian claystone (Cox) of the geologic repository (Figure 1a). The liner was meant to keep the borehole circular, should the waste package be retrieved in any far future. It was not designed for tightness, and so porewater, first filling the space between the liner and clay (Figure 1b), would later seep in, and lead to corrosion in a confined space gradually filled up with a reactive anoxic solution (Figure 1c). Thus, knowledge on the corrosion processes occurring under such confined conditions (i.e. where the reacting surface is surrounded by metal walls and sides, as opposed to surfaces plainly exposed to the clay matrix) was deemed mandatory.

A considerable number of studies have dealt with corrosion under HLW disposal conditions. Experiments were performed in laboratories [7-24], either on compact systems with a water flow, or in solutions or slurries with a reasonably high surface of steel exposed to water. These short-term (usually less than 10 years) laboratory studies were complemented by *in situ* investigations in deep underground laboratories [25-29], and by analyses of archaeological artefacts [30-36] or meteorites [37]. Surprisingly, little attention was devoted to the impact of partially confined anoxic conditions. Yet, in partially confined conditions, the solution composition is expected to be controlled by the interplay between slow diffusive or advective transport and corrosion/alteration reactions. The same limitations on transport are expected to affect the formation and corrosion in steel cracks and crevices. Finally, the impact of gradual filling has been entirely unexplored.

The present study focuses on the corrosion of C-steel in two examples of confined environments. One corresponds to a simulated crevice between two C-steel rods, a situation encountered either between two liner sections or for hypothetical overpack crevices. In this case, porewater should diffuse along

the crevice surface. The other case corresponds to an end-sealed, perforated C-steel tube (envelope) containing a C-steel rod, in order to simulate the situation where porewater would reach the overpack through the liner after clay percolation. In that case, porewater renewal is limited by transport through holes in the envelope. These specimens were reacted for more than six years at 90 °C (the peak temperature expected for the repository) under anoxic conditions in water-saturated Cox in a dedicated setup [38], under constant slow flux of water in equilibrium with clay. These experiments extend and complete previous observations made on shorter time scales [39]. Corrosion damage was assessed by weight loss, and the nature and distribution of corrosion products (CPs) by microscale investigations. The results show how the respective kinetics of transport and precipitation of porewater solutes within confined spaces results in CPs heterogeneity, ultimately controlling the formation of protective layers under anoxic clay conditions.

2 Materials and methods

2.1 Experimental setup

The experimental setup has been detailed in a companion paper [38]. Briefly, samples of A37 C-steel with various geometries were inserted in cylindrical Cox bricks within high-pressure cells (Figure 2a), fed with anoxic synthetic clay porewater [12], and heated at 90 °C for several months to years. Three types of sample geometries were investigated. Type 1 was a massive rod (diameter 10 mm, length 30 mm), the steel-clay interface of which was already investigated [38]. Type 2 was made of two head-on short rods (lengths of 14 and 15 mm) separated by a polytetrafluoroethylene (PTFE) disk (9 mm diameter, 1 mm thickness), and was designed to investigate corrosion in a crevice configuration (Figure 2b). Type 3 was made of an A37 tube with welded lids (length 30 mm, outer diameter 16 mm), pierced with six 2 mm-diameter holes and containing an A37 rod (diameter 8 mm, length 20 mm) centered with PTFE rings (Figure 1b,c). The rings prevented any contact between the internal rod and the tube or lids, and so hindered galvanic coupling. These specimens, thereafter referred to as “cover integrity loss” (CIL), were investigated to understand corrosion in confined volumes (Figure 1a, bottom right). These volumes differ from the simulated crevices by the greater metal-to metal distance (3 mm). Samples were collected after given exposure times (7, 15, 27, 40 and 76 months). One type 2 sample was quickly saved

in a glove box for characterization, and the others were used for gravimetric assessment of the average corrosion depth. In the case of the CIL specimens, only the internal rod were used for gravimetric measurements, and only specimens for 40 and 76 months were kept for microcharacterization.

2.2 Sample preparation and microcharacterization

Samples saved for microcharacterization were impregnated with resin, sectioned, and the cross-sections polished down to 1 µm using diamond paste, as described elsewhere [38]. Thin sections for transmission micro X-ray diffraction (µXRD) were obtained by polishing thin slices down to 100 µm thickness, and mounted on a sample holder under anoxic conditions [28, 29].

Optical images and micro Raman (µRaman) spectra were collected on cross-sections kept in airtight boxes with a glass window. Microphotographies were obtained with an Olympus BX51M equipped with a CCD camera (Sony Exwave HAD) and operated with the analySIS software. Micro Raman spectroscopy (µRS) was carried out on microspectrometers (Renishaw Invia and LabRam HR800) with excitation wavelengths of 532 or 785 nm and low power outputs (≥ 500 µW) to avoid solid overheating. Scanning electron microscopy (JEOL JSM7000-F) was performed on carbon-coated samples at 10 kV and 1.6-2 nA. Energy-Dispersive X-ray (EDX) spectra were collected on Points of Interest (PI) with a silicon-drift detector (Bruker XFlash 5010) and processed as described elsewhere [38]. Quantifications are given in atomic percent (at.%), and are rounded to two significant digits in the text. Elemental maps were recorded by sample continuous scanning and adding the EDX raw counts on each pixel. The µXRD data were recorded in transmission mode, with a Mo Kα rotating anode source (wavelength of 0.70932 nm), a focused X-ray beam (30×50 µm, vertical×horizontal), and a 2D Image plate detector (GE Healthcare).

3 Results

3.1 Weight loss

Figure 3 shows the evolution of the average corrosion depth with reaction time for half-rods mimicking a crevice (Figure 3a), and for the CIL internal rod (Figure 3b). The average corrosion depth

for the half-rods (crevice configuration) equals 10.5 ± 2.2 µm after seven months of corrosion. It then increases at a constant rate, up to 25.4 ± 2.2 µm after 76 months of reaction. This trend was tentatively fitted by linear, power, or logarithmic laws. As previously observed [38], the logarithmic law yielded the worst agreement and was discarded. The linear law provided a good estimate of the long-term trend, avoiding to take into account the initial, probably high corrosion rate, and could be described by:

$$D_{CLL} = 8.7\ (\pm\ 2.1) + 3.2\ (\pm\ 0.8) \times t\ , \qquad (1)$$

where D_{CLL} is the average corrosion depth for crevice samples (in µm) and t is the exposure time (in years).

The linear corrosion rate (3.2 ± 0.8 µm/year) compares with the value obtained for massive rods in contact with clay (3.5 µm/year; [38]). Because about 87 % of the half-rod is in contact with clay, the similarity in rates suggests that damage in the simulated crevice is probably limited. At the highest, it would be of about the same order of magnitude as for the steel-clay interface. Optical microscope and SEM observations of the crevice mouths beneath and around the PTFE disc did not reveal any localized corrosion features.

For the internal rod of the CIL specimen, the average corrosion depth is more limited for short reaction times (3.3 and 5 ± 1 µm at 7 and 27 months of reaction, respectively), probably due to delays needed by pore water to reach the internal rod itself. The long-term trend is blurred by the scatter between the values measured after 40 months of reaction (17.5 µm) and at the end of the experiment (11.5 µm at 76 months of reaction). This difference is larger than the estimated uncertainty in measurements (± 1 µm). Since only one rod was weighted (the other internal rod was kept for analyses), the origin of this scatter is unknown. Nevertheless applying the affine relationship on these points yields:

$$D_{\mu cLL} = 1.8\ (\pm\ 4.8) + 2.0\ (\pm 1.6) \times t\ . \qquad (2)$$

As expected from the scatter in values of average corrosion depths, parameters are affected by large uncertainties. However, most of the scatter is due to a single outlier at 40 months.

3.2 Microstructural characterization

3.2.1 Corrosion at simulated crevices

Electron micrographs show that corrosion within the simulated crevices is generally very limited, with little roughening of the metal surface (Figure 4) and depressions shallower than 20 µm. The corroded steel is covered by thin layers of CPs, with a thickness of less than 5 µm. This layer is compact and usually tightly bound to the metal surface. For short exposure times (7 to 27 months), the layer is homogeneous, with a composition dominated by O (74-78 at.%), Mg (1.2-12 at.%), Ca (0.4-6.3 at.%), and Fe (14-19 at.%). The cationic composition and the O / (Fe + Mg + Ca) ratios suggest the formation of hydroxylated or carbonated Fe compounds, i.e. (Mg, Ca)-doped siderite (ankerite). Locally, a slight enrichment in Si could be observed (up to 4 at.%), possibly related to the presence of Fe silicate. The presence of Mg, Ca and Si demonstrates that clay porewater with dissolved elements has been percolating along the crevice. For higher exposure durations (≥ 40 months), two successive layers are present (Figure 5). The inner layer contains essentially O, Fe, and Si, with a small amount of S. The composition of this inner layer (11-15 at.% Si, 23-28% Fe, 58-59 at.% O, 1.1-1.4 at.% S; Table 2, PI 1-3) suggests the formation of mostly Fe silicate phase. The outer layer (Table 2, PI 4-6) has a composition comparable to that of the early CPs, and is made of ankerite, as shown by µXRD performed on a thin slice (b). In conclusion, the nature of the CPs in the crevice indicated that corrosion, albeit much limited compared to steel surfaces in direct contact with clay, occurred in presence of porewater.

3.2.2 Corrosion inside the CIL setup

That the CIL specimens were only gradually filled by porewater (through the drilled holes in the external tube) is evident from the presence of water marks on the inside and on the internal rods for short exposure times (e.g. 15 months; Figure 6a). For longer exposure times, these marks are no longer observed (Figure 6b), attesting to a complete filling of the tube with solution. Cross-sections show that the inside surface of the tube wall (inside wall) and of the internal rod are heterogeneously corroded (Figure 7a-f). The presence of clay minerals near part of the inside wall is interpreted as resulting from clay penetration and settling. This allows identifying the bottom part of the CIL specimen (Figure 7 a,d). It is then possible to remark that steel damage in the bottom parts (up to 100 µm after 40 months; Figure

7a) is more important than on the upper parts (up to 35 µm after 76 months; Figure 7f). This suggests that the lower and upper inside walls experienced distinct conditions, in line with immersion of the lower wall occurring first. According to SEM cross-sections examined along the lower inside wall, corrosion depth is usually found around 35-40 µm, locally as deep as 100 µm after 40 months exposure. Corrosion is comparatively more limited on the upper inside wall, with 25 µm on average and locally as deep as 60 µm after 76 months (Figure 7c,f). The corrosion of the internal rod is intermediate in nature and magnitude between those of the upper and lower walls (Figure 7b,e). The average corroded metal depth from SEM analyses equals about 10 µm and 5 µm after 40 and 76 months exposure, respectively. Some straight-faced depressions as deep as 20 µm are visible along the interface, which may correspond to local higher oxidation rates associated with favourable orientation of steel grains.

The steel-CPs interface is significantly jagged, attesting to the heterogeneous nature of the corrosion interface. Nonetheless, no specific feature of any localized corrosion process (intergranular oxidation or pitting) is observed. In addition, for all interfaces, several successive units of CPs can be identified. The innermost layer of CPs forms at the expense of metal; hence, it corresponds to a Dense Products Layer (DPL). The trace of the metal initial surface is visualised by a discontinuous median corrosion layer (MCL), with a thickness of a few µm. A layer of outer corrosion products (OCPs) can then be observed with contrasted morphologies, either as CPs mixed with clay (Figure 7a,d), or as massive layers (Figure 7b,c,e,f), sometimes protruding outer filamentous crystallites (Figure 7b,c). The nature of the CPs units has been thoroughly investigated to understand the control of corrosion reactions in the liner-overpack interspace.

Chemical mapping (Figure 8.a) and quantitative analysis (Table 3) of the lower inside wall after 40 months of exposure show that the DPL essentially contains O and Fe (Table 3, PI-1-6), with a significant local enrichment in Si for the DPL most external fringe (up to 20 at.%; Table 3, PI 5-6). Detailed analysis shows the coexistence of three types of crystalline solids. The first type has a very high Fe content and comparatively low O content (40-44 and 54-55 at.% respectively ; Table 3, PI 1-2) and is identified by µRS as magnetite (Figure 8.b, PI a,b). The second type has a lower Fe content and a higher O content (33-35 and 62-63 at.% respectively; Table 3, PI 3-4), and is identified as chukanovite (Figure

8.b, PI c). Interestingly, chukanovite is slightly enriched in S (up to 1.2 at.%), a preferential association which was also observed in corrosion layers developed in clayey water [28]. The third type of solid would correspond to Fe silicate phases, for which there is no Raman signal [38]. The trace of the original surface presumably coincides with the Si-enriched thin layer (17-20 at.%). The Fe-rich solids present as outer CPs (OCPs) display measured O/Fe ratios quite comparable to that of magnetite, but due to the heterogeneity and porosity of this layer, the EDX quantification may be unreliable. Local µRaman spectra showed bands near 250, 300, and 395 cm^{-1} (Figure 8b, PI d), near the positions observed for goethite (α-FeOOH), yet Raman bands at higher wavenumbers expected for goethite were not observed. In fact µXRD patterns of this area (not shown) suggest the predominance of magnetite and the presence of siderite. Finally, the outermost material is a mixture of clay material cemented by siderite with a remarkably low Ca content (less than 0.6 at.%).

On the upper inside wall, after 40 months exposure, an internal (Fe, O) layer is observed with an O/Fe ratio suggesting magnetite (Figure 9 and Table 4, PI 1). An intermediate (Fe, Si, O) layer is also observed, with a Si content of ~17-18 at.% (Figure 9 and Table 4, PI 2 to 4). This layer is in contact with an external Fe-rich layer with locally some Ca (Table 4, PI 5 to 7) suggesting the formation of ankerite. The most external layer has a radial fibrous-like morphology with some round precipitates, and is made of O and Fe (possibly C and H). Insight into the nature of these solids composing the outermost layer was actually obtained from the investigation of the internal rod.

After 40 months corrosion, the internal rod displays some depressions filled with magnetite (see µRaman spectrum at PI a; Figure 10b). The innermost layers in contact with steel contain essentially Fe (29 at.%) and O (67 at.%; Table 5), suggesting an Fe (hydr)oxide or hydroxycarbonate. There is a possibility that this very thin layer extends laterally on the whole metal-oxide interface. The next layer (MCL in Figure 10a) is made of a 7 µm thick Si-rich fringe (Si content between 15 and 17.5 at.%). This layer is in contact with another (Fe, O) unit, the Fe content of which gradually decreases with increasing distance to steel (Table 5, PI 5-8). The Ca content of these layers is quite variable (0.4-6.8 at.%), hinting at the possible local presence of siderite and ankerite. Indeed, µRS reveal the presence of Fe-rich carbonate (peak near 1088 cm^{-1}), and also of chukanovite (peak near 1071 cm^{-1}; Figure 10b, PI b).

206 Finally, the most external layer is made of well-separated minerals appearing as filamentous on the
207 cross-section, with an increasing porosity from steel to the environment. Surprisingly, the O:Fe ratio of
208 these minerals, measured by EDXS, is around 55:45, a value typical of magnetite. Locally, these layers
209 contain (Ca, Fe) rich nodules, identified by µRS as ankerite (Figure 10b, PI c).

210 Similar observations can be made on the nature and distribution of CPs for the 76-months sample
211 (Figure 7d-f). One notable difference is that only magnetite is detected in the DPL layer for all parts of
212 the tube inside walls, as well as for the internal rod. Also, OCPs made of siderite are observed for the
213 lower wall. The upper wall is more corrugated, with enlargement of several oxide penetrations over
214 distances of a few tens of µm (Figure 7f). In addition, the Si-rich fringe on this sample is not continuous,
215 suggesting it has not formed at the same rates on the T40 (40 months) and T76 (76 months) samples, or
216 that it has partially dissolved on the T76 sample. Thus, although the whole inside wall was in contact
217 with solution for more than three years, the discrepancy between the bottom and top part of this wall
218 persisted throughout the exposure time.

219 # 4 Discussion

220 ## *4.1 Steel corrosion in the crevice configuration*

221 Compared to steel surfaces in direct contact at 80-90 °C with clay [38], bentonite [40], or porewater
222 [27, 28], the corrosion damage in the simulated crevices is quite limited. Even after 76 months of
223 exposure to the media, the thickness of corroded steel and of corrosion layers are both limited to a few
224 µm (Figure 4). The little CPs (a few µm) present within the crevices are made of Fe (hydr)oxide or
225 carbonate, and Fe silicate. The presence of silicate, which could be transported only in dissolved (or
226 colloidal) form, indicates that fluids have penetrated deep in the crevice.

227 One hypothesis for this near-absence of CPs is that the surface does corrode, but that oxidized Fe is
228 transported away by diffusion instead of precipitating *in situ*. In that case, however, corrosion would
229 likely have resulted in greater surface roughening, which is not observed here. Thus, the absence of CPs
230 probably results from limited corrosion, or to limited transport of water and reacting species in the
231 crevice. Under anoxic conditions, a protecting layer would remain stable because of basic pH [41, 42],

and of the low concentrations of ligands such as carbonate and silicate. It may however be destabilized by the presence of chloride [43]. In addition, the presence of CPs on the whole crevice surface buffers the concentation of dissolved Fe to the solubility of these solids, thus decreasing lateral gradients and hindering outward transport of Fe. Thus, it seems that the corrosion rate is limited by the slow dissolution rate of the protective CPs, related to rather steady chemical conditions and to a limited ingress of reactive species.

Finally, it is worth mentioning that the corrosion mechanism within these model crevices differs from those usually observed in oxic environments, in which a significant oxygen gradient can occur. Such gradients can favor the onset of spatial decoupling between cathodic reactions on the external surfaces near the crevice lips, and anodic reactions in deep, oxygen-deprived areas. Here a strong gradient in oxidizing species can be ruled out, because water was everywhere, including in the crevice. Spatial decoupling could also have been favored by a difference in CPs composition beween the crevice and the clay-contacting surfaces. This is the case e.g. in cement grouts, in which localized corrosion correlates with the presence of cathodic magnetite and anodic mackinawite areas [44]. Here, the distribution of sulfide compounds near the clay-steel interface [38] and Fe-(hydr)oxide or silicate (within the crack) actually runs counter to the expected galvanic coupling, thereby further hindering extended crevice corrosion.

4.2 The effect of partial confinement of pore solution in the liner – overpack interspace on the heterogeneity of steel corrosion

Our analysis of the time dependence of corrosion interfaces within the CIL specimen, i.e. tube-internal rod space mimicking the liner-overpack interspace, is limited by the fact that only containers reacted for 40 and 76 months were investigated at the microscopic scale. Thus, any evolution from the short-term features can only be speculated from these long-term observations. It is however possible to assess the relative importance of short-term (atmospheric) and long-term aqueous corrosion in the partially confined environment of the liner-overpack interspace. Note that here confined environment

refers to relatively stagnant porewater in the interspace because this solution is out of the main stream imposed through the set-up (Figure 2a).

Initial corrosion in this interspace is expected to occur by atmospheric oxidation of steel in humid air, at least until all O_2 is captured to form CPs. The amount of CPs that can form can be estimated from the amount of O_2 in the trapped volume and from the simple mass balance of iron oxidation to form magnetite:

$$3\ Fe^{(0)} + 2\ O_2 \rightarrow Fe_3O_4\ . \qquad (3)$$

Although this relationship does not involve water, the presence of water is required under ambient to moderate conditions for corrosion to occur at a significant rate. The residual amount of O_2 in the interspace calculated assuming closure at room temperature approximates 26 µmol. The amount of steel (assumed as pure Fe here for simplicity) that can be oxidized by O_2 is then readily estimated from the volumic mass and the molar mass of iron (about 7.87 g/cm^3 and 55.845 g/mol, respectively) and equals about 0.8 mm^3. Assuming corrosion is homogeneously distributed over the entire internal surface of steel (i.e. the tube inside walls and the internal rod), the final thickness of corroded iron is thinner than 0.15 µm, two orders of magnitude lower than the observed average corrosion depth. The overall fraction of the corrosion damage due to atmospheric corrosion is thus expected to be marginal.

Additional insight into the corrosion mechanism can be obtained from the morphology of the corrosion front and the spatial heterogeneities of CPs within the interspace. The internal walls of the tube are notably distinct from the steel-clay interface in terms of morphology of corrosion layers. One key difference is that the nature of the corrosion interface depends on the area location along the inside wall (difference between lower and upper parts). This contrasts with the seemingly random distribution of significantly and sparingly corroded areas over the entire outer surface of the tube (i.e. in direct contact with water-saturated clay) [38]. Second, magnetite and chukanovite predominate in the inside wall and the internal rod DPL, and they are present as massive domains. Silicate CPs also form in the DPL close to the trace of the original steel surface, but the relatively limited proportion does not compare with the thick layers observed at the steel-clay interface [38]. Since all physical (P, T) parameters were identical for the tube inside and outer surfaces, this discrepancy likely reflects distinct chemical and transport

284 conditions in the tube-internal rod interspace. At the steel clay interface (tube outer surface), porewater
285 can react with clay within a few mm from the steel surface, and dissolved elements can then readily
286 diffuse to and from the interface. Stated another way, exchange fluxes between clay and corrosion layers
287 can occur over the entire steel-clay interface, being limited only by diffusion in clay and corrosion layers.
288 In contrast, the interspace solution diffuses through six small holes of about 2 mm in diameter (after
289 diffusion in the nearby clay), hence a total surface of about 19 mm^2. This is two orders of magnitude
290 smaller than the metal surface in the interspace (about 1500 mm^2 counting the internal rod and tube
291 inside wall). Given this small ratio, a limited supply of dissolved species such as silicate, Ca or Mg is
292 expected within the interspace compared to the outer steel-clay interface. Part of the Si species observed
293 in the corrosion products may be supplied by the pore water itself, and also by the little amount of clay
294 that dropped through the holes into the interspace. However this supply is probably limited by clay
295 solubility, and by the overall low total surface of minerals. Overall, the formation of all other CPs
296 (except Fe (hydr)oxides) is probably subject to comparable limitations in supply of dissolved elements.

297 Another discrepancy is observed between the bottom and top parts of the tube inner wall. This
298 discrepancy persisted over the exposure time, in spite of full immersion of the inner wall over more than
299 three years. This suggests that the initial differences in early stages of corrosion significantly influence
300 future years and exposure. A possible explanation is that extended corrosion occurred at the lower walls
301 first, somewhat slowing down the flux of water toward the steel surface. Later, as the whole tube was
302 filled, the near-direct contact between steel and solution at the upper part favored the cathodic reaction of
303 water reduction. A galvanic coupling then occurred between the upper and lower parts, resulting in
304 separation between anodic and cathode reactions, and in some protection of the upper walls.

305 Interestingly, steel damage of the tube lower inside wall seems to be of the same order of magnitude
306 (30-40 µm after 76 months) than at the steel-clay interface (average corrosion depths of 29 ± 3 and 43 ±
307 21 µm estimated from gravimetric and direct microscopic measurements, respectively; [38]). This
308 similarity contrasts with the distinct morphologies of corrosion interface. Indeed, at the steel-clay
309 interface, metal-replacing CPs are restricted to several depressions and to a thin (2-3 µm) layer of
310 siderite. In contrast, the tube lower walls are more homogeneously corroded. This suggests that

magnetite at the inner wall, however thick, is less protective [45]. The absence of such a thick oxide layer at the steel-clay interface then directly relates to the destabilization of magnetite by silicate [12].

Compared to the specimen reacted for 40 months, the most interesting result for the DPL of the 76-month inside wall is the absence of chukanovite. However, because of the confined nature of water in the interspace, it is unclear if similar chemical conditions prevailed in the two specimens at 40 and 76 months. In fact, due to the small relative area of the water inlets, small variations in hole permeability (e.g. by clay clogging or corrosion products extension at the holes) would have easily resulted in distinct compositions of the internal solutions. Another evidence for distinct chemical conditions is given by the composition of the siderite layer, which is significantly doped in Ca at 40 months, and not so much at 76 months. The absence of chuckanovite may also reflect an evolution of the interspace solution toward the magnetite/siderite thermodynamic equilibrium.

Finally, our results indicate that the corrosion facies for internal rods at 40 and 76 months are fairly similar, meaning the corrosion rates should be consistent with each other. This expected similarity contrasts with the scatter in the average corrosion depths observed from weight loss measurements. Several hypotheses were examined to explain this discrepancy. Localized corrosion is ruled out, because local SEM cross-sections on geuine specimens and optical observations carried out after desquamation, albeit difficult to interprete, did not reveal any trace of pit-like corrosion. Another hypothesis is a possible high variability in the surface microstructure of the internal rod, due e.g. to different surface pearlite-to-ferrite ratios. In fact, optical and SEM observations on cross-sections suggest that CPs volumes are larger aroud pearlite islands compared to ferrite grains, suggesting differential corrosion due to some galvanic coupling. Distinct corrosion rates would then relate to distinct pearlite-to-ferrite ratios exposed at the surface from the preparation stage of the specimens (before corrosion). Further investigations are nonetheless required to better understand this discrepancy. Note however that this scatter, though quite significant, may actually account for the variability in overall corrosion damage.

4.3 Implications for the long-term corrosion of steel in deep geological environments

The absence of important CPs modifications between 40 and 76 months suggests that the same mechanism operated during this time span, and probably would for longer corrosion times. This implies that a (pseudo-) stationary regime has been attained after 76 months, with the low corrosion rate not expected to increase anymore. Thus the rate laws proposed from the weight loss measurements may be used to provide a rough estimate of the steel damage at 90 °C for anoxic conditions. From equation (2), the average corrosion depth calculated for the internal rod after 10, 100 and 1000 years equal 22 (±21), 202 (± 170), and 2002 (± 1600) µm, respectively. Note that most of the uncertainty derives from the outlier at 40 months. Another value, namely greatest corrosion depth, could be extrapolated from the greatest depths obtained from SEM observations on cross-sections. However, too few data were available to propose any trend, as suggested by the erratic extrema reported here (greatest depths of 100 µm after 40 months and 60 µm after 76 months). In addition, no information is available on the propagation kinetics of the oxidation front at these areas, which further hinders any interpretation. Furthermore, it has been shown that the ratio of maximum depth over average damage for anoxic corrosion of C-steel is bounded by a semi-empirical value which steadily decreases over time [46, 47]. This upper limit is somewhat corroborated by our results showing little corrosion in the simulated crevice. Note that no trace of actual pitting was observed, minimizing the possibility of local accelerated corrosion that could be critical for the overpack integrity. This lends additional confidence to our extrapolations of average corrosion depths over long times.

An additional source of uncertainty is the hypothesis that the system will not evolve much during this long period of time, i.e. has already reached a quasi-stationary regime after 40 or 76 months. Finally, how these corrosion rates obtained under in laboratory-controlled experiments may compare to real in-field (fluctuating) conditions still has to be assessed. For example, a stationary regime suggests that rates of iron corrosion and reactant diffusion in stable geologic environments are not expected to vary much. However, temperature fluctuations in tight geologic systems may occur over only long timescales (years to centuries). A temperature decrease could in fact result in an increase in the corrosion rate as corrosion

362 in such complex systems is controlled by the rates of steel oxidation and CPs precipitation [48].
363 Modelling in pure carbonate systems predicted that the rate of CPs precipitation decreases more rapidly
364 than that of steel oxidation as the temperature decreases towards ambient conditions [48]. Such
365 calculations however do not take into account the diffusion of reactants and products in compact clay,
366 which is usually temperature-activated and can significantly influence the corrosion rate [38].

367 5 Concluding remarks

368 Corrosion within simulated crevices and in the liner-overpack interspace (tube inside walls and internal
369 rod) somewhat differs from that of the steel-clay interface. First, areas with the greatest damage are not
370 randomly distributed, but are located essentially where steel is wetted first by porewater. The resulting
371 contrast between areas of extensive and limited corrosion persists even after six years, an indication that
372 subsequent corrosion is controlled by the initial damage. Damage heterogeneity also affects the internal
373 rod in the setup, but to a smaller extent, possibly because the transition from partial to full wetting was
374 more rapid. The DPL is essentially made of magnetite, a mineral which is usually believed to form
375 protective layers at the steel surface. However, here, magnetite coincides with areas of highest damage
376 and presumably has little protective effect. Second, relatively limited amounts of silicate and carbonate
377 solids have formed in the interspace, compared to the extensive amounts present at the steel-clay
378 interface. Because the systems are subject to homogeneous pressure and temperature conditions, this
379 contrast can be explained only by lower solution concentrations of elements (Si, Ca) in this interspace.

380 In spite of these spatial heterogeneities, the greatest sample damage after six years remains significantly
381 smaller than values measured in the porewater [28, 29], attesting to surface protection, and compares
382 with what was found for steel-clay compact interfaces. This is probably because diffusion, either through
383 the tube holes or in the bulk clay, significantly limits the transport of reactants toward corrosion sites.
384 Thus it seems that limiting water fluxes is key to limiting steel corrosion, even in the presence of
385 fluctuations in water content, composition, and temperature.

6 Acknowledgements

The authors gratefully acknowledge the financial support of Andra and EdF for experimental work and results interpretation. D. Crusset, F. Foct, J.M. Gras and members of the GL "Verre-Fer-Argile" are also gratefully acknowledged for fruitful discussions on the setup definition and on scientific results. Claude Gatabin is thanked for extraction the samples from the high-pressure cells. The fruitful contribution of three anonymous reviewers is acknowledged.

Data availability

The raw/processed data required to reproduce these findings cannot be shared at this time due to legal reasons.

Declaration of interest

The authors declare no conflict of interest.

References

[1] G. De Marsily, E. Ledoux, A. Barbreau, J. Margat, Nuclear waste disposal: can the geologist guarantee isolation?, Science, 197 (1977) 519-527.

[2] K.B. Krauskopf, Aqueous geochemistry of radioactive waste disposal, Appl. Geochem., 1 (1986) 15-23.

[3] M. Sawiki, Council Directive 2011/70/EURATOM of 19 July 2011 establishing a Community framework for the responsible and safe management of spent fuel and radioactive waste, Off. J. Europ. Union, 199 (2011) 48-56.

[4] F. King, Waste containers, in: T.R. Allen, R.E. Stoller, S. Yamanaka (Eds.) Material performance and corrosion waste materials, Elsevier, Amsterdam, 2012, pp. 421-450.

[5] F. King, Container materials for the storage and disposal of nuclear waste, Corrosion, 69 (2013) 986-1011.

[6] Andra, Evaluation de la faisabilité du stockage géologique en formation argileuse, in, Andra, Chatenay-Malabry, France, 2005, pp. 240.

[7] F.T. Madsen, Clay mineralogical investigations related to nuclear waste disposal, Clay Min., 33 (1998) 109-129.

[8] L. Carlson, O. Karnland, V.M. Oversby, A.P. Rance, N.R. Smart, M. Snellman, M. Vahanen, L.O. Werme, Experimental studies of the interactions between anaerobically corroding iron and bentonite, Phys. Chem. Earth, 32 (2007) 334-345.

[9] N.R. Smart, A.P. Rance, L.O. Werme, The effect of radiation on the anaerobic corrosion of steel, J. Nucl. Mater., 379 (2008) 97-104.

[10] C. Bataillon, C. Musy, M. Roy, Corrosion des surconteneurs de déchets, cas d'un surconteneur en acier faiblement allié., J. Phys. IV, 11 (2001) 267-274.

[11] F.A. Martin, C. Bataillon, M.L. Schlegel, Corrosion of iron and low alloyed steel within a water saturated brick of clay under anaerobic deep geological disposal conditions: An integrated experiment, J. Nucl. Mater., 379 (2008) 80-90.

[12] M.L. Schlegel, C. Bataillon, K. Benhamida, C. Blanc, D. Menut, J.-L. Lacour, Metal corrosion and argillite transformation at the water-saturated, high temperature iron-clay interface: a microscopic-scale study, Appl. Geochem., 23 (2008) 2619-2633.

[13] M.L. Schlegel, C. Bataillon, C. Blanc, D. Prêt, E. Foy, Anodic activation of iron corrosion in clay media under water-saturated conditions at 90 °C: characterization of the corrosion interface, Environ. Sci. Technol., 44 (2010) 1503-1508.

[14] G. de Combarieu, P. Barboux, Y. Minet, Iron corrosion in Callovo-Oxfordian argilite: From experiments to thermodynamic/kinetic modelling, Phys. Chem. Earth, 32 (2007) 346-358.

[15] G. de Combarieu, M.L. Schlegel, D. Neff, E. Foy, D. Vantelon, P. Barboux, S. Gin, Glass-Iron-Clay interaction in a radioactive waste geological disposal: an integrated laboratory-scale experiment, Appl. Geochem., 26 (2011) 65-79.

[16] Y. El Mendili, A. Abdelouas, J.F. Bardeau, Insight into the mechanism of carbon steel corrosion under aerobic and anaerobic conditions, Phys. Chem. Chem. Phys., 15 (2013) 9197-9204.

[17] Y. El Mendili, A. Abdelouas, J.F. Bardeau, Impact of a sulphidogenic environment on the corrosion behavior of carbon steel at 90°C, RSC Adv., 3 (2013) 15148-15156.

[18] Y. El Mendili, A. Abdelouas, A.A. Chaou, J.F. Bardeau, M.L. Schlegel, Carbon steel corrosion in clay-rich environment, Corros. Sci., 88 (2014) 56-65.

[19] Y. El Mendili, A. Abdelouas, G. Karakurt, A.A. Chaou, R. Essehli, J.F. Bardeau, J.M. Greneche, The effect of temperature on carbon steel corrosion under geological conditions, Appl. Geochem., 52 (2015) 76-85.

[20] S. Kaufhold, A.W. Hassel, D. Sanders, R. Dohrmann, Corrosion of high-level radioactive waste iron-canisters in contact with bentonite, J. Hazard. Mater., 285 (2015) 464-473.

[21] S. Kaufhold, R. Dohrmann, Distinguishing between more and less suitable bentonites for storage of high-level radioactive waste, Clay Min., 51 (2016) 289-302.

[22] Y. Leon, M. Saheb, E. Drouet, D. Neff, E. Foy, E. Leroy, J.J. Dynes, P. Dillmann, Interfacial layer on archaeological mild steel corroded in carbonated anoxic environments studied with coupled micro and nano probes, Corros. Sci., 88 (2014) 23-35.

[23] M. Robineau, A. Romaine, R. Sabot, M. Jeannin, V. Deydier, S. Necib, P. Refait, Galvanic corrosion of carbon steel in anoxic conditions at 80 °C associated with a heterogeneous magnetite (Fe_3O_4)/mackinawite (FeS) layer, Electrochim. Acta, 255 (2017) 274-285.

[24] A. Romaine, M. Jeannin, R. Sabot, S. Necib, P. Refait, Corrosion processes of carbon steel in argillite: Galvanic effects associated with the heterogeneity of the corrosion product layer, Electrochim. Acta, 182 (2015) 1019-1028.

[25] S. Necib, N. Diomidis, P. Keech, M. Nakayama, Corrosion of carbon steel in clay environments relevant to radioactive waste geological disposals, Mont Terri rock laboratory (Switzerland), Swiss J. Geosci., 110 (2017) 329-342.

[26] S. Necib, Y. Linard, D. Crusset, M. Schlegel, S. Daumas, N. Michau, Corrosion processes of C-steel in long-term repositories conditions, Corr. Eng. Sci. Technol., 52 (2017) 127-130.

[27] S. Necib, Y. Linard, D. Crusset, N. Michau, S. Daumas, E. Burger, A. Romaine, M.L. Schlegel, Corrosion at the carbon steel-clay borehole water and gas interfaces at 85°C under anoxic and transient acidic conditions, Corros. Sci., 111 (2016) 242-258.

[28] M.L. Schlegel, S. Necib, S. Daumas, C. Blanc, E. Foy, N. Trcera, A. Romaine, Microstructural characterization of carbon steel corrosion in clay borehole water,under anoxic and transient acidic conditions, Corros. Sci., 109 (2016) 126-144.

[29] M.L. Schlegel, S. Necib, S. Daumas, M. Labat, C. Blanc, E. Foy, Y. Linard, Corrosion at the carbon steel-clay borehole water and gas interfaces at 85 °C under anoxic alkaline conditions, Corros. Sci., 136 (2018) 70-90.

[30] D. Neff, P. Dillmann, L. Bellot-Gurlet, G. Berranger, Corrosion of iron archaeological artefacts in soil : characterisation of the corrosion system, Corros. Sci., 47 (2005) 515-535.

[31] D. Neff, P. Dillmann, M. Descostes, G. Beranger, Corrosion of iron archaeological artefacts in soil: Estimation of the average corrosion rates involving analytical techniques and thermodynamic calculations, Corros. Sci., 48 (2006) 2947-2970.

[32] D. Neff, M. Saheb, J. Monnier, S. Perrin, M. Descostes, V. L'Hostis, D. Crusset, A. Millard, P. Dillmann, A review of the archaeological analogue approaches to predict the long-term corrosion behaviour of carbon steel overpack and reinforced concrete structures in the French disposal systems, J. Nucl. Mater., 402 (2010) 196-205.

[33] D. Neff, E. Vega, P. Dillmann, M. Descostes, L. Bellot-Gurlet, G. Beranger, Contribution of iron archeological artefacts to the estimation of average corrosion rates and the long-term corrosion mechanisms of low-carbon steel buried in soils, in: P. Dillmann, G. Beranger, P. Piccardo, H. Matthiesen (Eds.) Corrosion of metallic heritage artefacts, Woodhead, Cambridge, UK, 2007, pp. 41-76.

[34] M. Saheb, D. Neff, P. Dillmann, H. Matthiesen, E. Foy, Long-term corrosion behaviour of low-carbon steel in anoxic environment: characterization of archaeological artefacts, J. Nucl. Mater., 379 (2008) 118-123.

[35] M. Saheb, M. Descostes, D. Neff, H. Matthiesen, A. Michelin, P. Dillmann, Iron corrosion in an anoxic soil: Comparison between thermodynamic modelling and ferrous archaeological artefacts characterised along with the local in situ geochemical conditions, Appl. Geochem., 25 (2010) 1937-1948.

[36] M. Saheb, D. Neff, L. Bellot-Gurlet, P. Dillmann, Raman study of a deuterated iron hydroxycarbonate to assess long-term corrosion mechanisms in anoxic soils, J. Raman Spectrosc., 42 (2011) 1100-1108.

[37] G.A. Yakovlev, A.V. Chukin, V.I. Grokhovsky, V.A. Semionkin, M.I. Oshtrakh, Study of Dronino iron meteorite weathering in clay sand using Mossbauer spectroscopy, Croatica Chemica Acta, 89 (2016) 117-124.

[38] M.L. Schlegel, F. Martin, M. Fenart, C. Blanc, J. Varlet, E. Foy, D. Pret, N. Trcera, Corrosion at the carbon steel-clay compact interface at 90°C: insight into short- and long-term corrosion facies, Corros. Sci., 152 (2019) 31-44.

[39] F. Martin, S. Perrin, M. Fenart, M. Schlegel, C. Bataillon, On corrosion of carbon steels in Callovo-Oxfordian clay: complementary EIS, gravimetric and structural study providing insights on long term behaviour in French geological disposal conditions, Corr. Eng. Sci. Technol., 49 (2014) 460-466.

[40] T. Ishidera, K. Ueno, S. Kurosawa, T. Suyama, Investigation of montmorillonite alteration and form of iron corrosion products in compacted bentonite in contact with carbon steel for ten years, Phys. Chem. Earth, 33 (2008) S269-S275.

[41] M.K. Nieuwoudt, J.D. Comins, I. Cukrowski, The growth of the passive film on iron in 0.05 M NaOH studied in situ by Raman microspectroscopy and electrochemical polarization. Part II: In situ Raman spectra of the passive film surface during growth by electrochemical polarization, J. Raman Spectrosc., 42 (2011) 1353-1365.

[42] M.K. Nieuwoudt, J.D. Comins, I. Cukrowski, The growth of the passive film on iron in 0.05 M NaOH studied in situ by Raman micro-spectroscopy and electrochemical polarisation. Part I: near-resonance enhancement of the Raman spectra of iron oxide and oxyhydroxide compounds, J. Raman Spectrosc., 42 (2011) 1335-1339.

[43] C.S. Brossia, G.A. Cragnolino, Effect of environmental variables on localized corrosion of carbon steel, Corrosion, 56 (2000) 505-514.

[44] M. Robineau, R. Sabot, M. Jeannin, V. Deydier, D. Crusset, P. Refait, Mechanisms of localized corrosion of carbon steel associated with magnetite/mackinawite layers in a cement grout, Mater. Corros., senqsensen (2020) 1-17.

[45] C. Bataillon, F. Bouchon, C. Chainais-Hillairet, C. Desgranges, E. Hoarau, F. Martin, S. Perrin, M. Tupin, J. Talandier, Corrosion modelling of iron based alloy in nuclear waste repository, Electrochim. Acta, 55 (2010) 4451-4467.

[46] J.-M. Gras, Life prediction for HLW containers - issues related to long-term extrapolation of corrosion resistance, C.R. Physique, 3 (2002) 891-902.

[47] F. Foct, J.M. Gras, Semi-empirical model for carbon steel corrosion in long term geological nuclear waste disposal, in: International Workshop "Prediction of long term corrosion behaviour in nuclear waste systems", EFC, Cadarache, France, 2002.

[48] S. Nešić, M. Nordsveen, R. Nyborg, A. Stangeland, A mechanistic model for carbon dioxide corrosion of mild steel in the presence of protective iron carbonate films - Part 2: A numerical experiment, Corrosion, 59 (2003) 489-497.

7 Figure captions

Figure 1. (a) Schematic cross-section of the former design for disposal cells in the French High-level waste repository. (b) Illustration of the gradual filling of the space between clay and the liner. (c) Illustration of the confined interspace between the liner and the overpack, resulting in corrosion under confined conditions.

Figure 2. (a) Schematic illustration of the high-pressure cell setup and positioning of the samples. In real experiments, “crevice” and “cover integrity loss” (CIL) specimens were corroded in separate cells. (b) Illustration of the sample geometries.

Figure 3. Sample damage as a function of reaction time for the massive half-rods of the simulated crevices (a) and the steel rods within the CIL specimens (b). Also illustrated are the fits of experimental data with logarithmic law, power law and linear law.

Figure 4. Scanning electron images (BSE mode) showing the evolution of the corrosion interfaces in the simulated crevices as a function of reaction time. (a,b) C07 sample, 7 months. (c) C13, 13 months. (d) C27, 27 months. (e) C40, 40 months. (f) C76, 76 months.

Figure 5. (a) Chemical mapping of element distributions at the simulated crevice interface of the C40 rod (40 months of reaction). The dotted line marks the interface between inner and outer corrosion layers. (b) µXRD diagram of a thin slice of the simulated crevice.

Figure 6. (a) Optical images of the two envelopes and internal rods of the CIL specimens after 15 months of reaction time, showing the presence of water marks indicating gradual filling of porewater inside the envelope.

Figure 7. Scanning electron micrographs of the corrosion interfaces in the CIL setup for 40 (a-c) and 76 (d-f) months of reaction time. (a,d) Lower inside wall of the tube. (b,e) Central rod.

Figure 8. (a) BSE image and chemical mapping of element distributions at the lower inside wall of the CIL setup corroded for 40 months. DPL: dense products layer. MCL: median corrosion layer.

OCPs: outer corrosion products. (b) μRaman spectra at selected points of interest (PI) of the corrosion interface. The PI locations are indicated on the BSE image.

Figure 9. (a) BSE image and chemical mapping of element distributions at the upper inside wall of the CIL setup corroded for 40 months.

Figure 10. (a) BSE image and chemical mapping of element distributions for the corrosion interface of the central rod for the CIL setup corroded for 40 months. (b) μRaman spectra at selected points of interest (PI) of the corrosion interface. The PI locations are indicated on the BSE image.

8 Tables

Table 1. List of the samples investigated in this study.

Name	Reaction time	Sample type
C07	7 months	Crevice
C13	13 months	Crevice
C27	27 months	Crevice
C40	40 months	Crevice
T40	40 months	Tube + internal rod
C76	76 months	Crevice
T76	76 months	Tube + internal rod

Table 2. Quantification of SEM-EDX analyses for the artificial crevice of the C40 sample (40 months). The PI are indicated in Figure 5a.

Analysis	Composition (at. %)											
spot	O	Na	Mg	Al	Si	S	Cl	K	Ca	Fe	Cu	Zn
1	59.1	0.3	0.3	0.2	14.8	1.4	0.1	0.0	0.1	23.3	0.2	0.0
2	58.0	0.2	0.3	0.1	11.0	1.4	0.1	0.0	0.2	28.5	0.2	0.0
3	58.4	0.1	0.4	0.2	14.7	1.1	0.0	0.0	0.4	24.4	0.2	0.0
4	68.2	0.2	0.8	0.1	0.2	0.0	0.0	0.0	3.0	27.0	0.3	0.1
5	71.0	0.3	1.1	0.1	0.2	0.1	0.0	0.0	3.4	23.2	0.4	0.1
6	71.4	0.3	1.6	0.2	0.4	0.3	0.0	0.0	4.6	20.7	0.5	0.2

571

Table 3. Quantification of SEM-EDX analyses at the lower inside wall of the CIL setup reacted for 40 months. The PI are indicated in Figure 8a.

PI	Composition (at. %)									
spot	O	Na	Mg	Al	Si	S	Cl	K	Ca	Fe
1	53.6	0.2	0.3	0.2	0.6	0.4	0.0	0.0	0.1	44.5
2	55.2	0.3	0.4	0.3	3.3	0.2	0.0	0.0	0.0	40.2
3	62.1	0.4	0.4	0.2	0.6	1.2	0.0	0.0	0.1	34.9
4	62.8	0.4	0.4	0.3	1.9	1.1	0.0	0.1	0.1	33.0
5	60.7	0.4	0.5	0.3	17.4	0.5	0.3	0.0	0.1	19.8
6	52.1	0.1	0.4	0.3	19.6	0.6	0.2	0.0	0.0	26.8
7	54.1	0.2	0.3	0.2	1.8	0.2	0.4	0.0	0.2	42.5
8	51.5	0.2	0.4	0.2	2.1	0.3	0.5	0.0	0.2	44.6

572
573
574
575

Table 4. Quantification of SEM-EDX analyses at the upper inside wall of the CIL setup corroded for 40 months. The PI are indicated in Figure 9.

Analysis	Composition (at. %)									
spot	O	Na	Mg	Al	Si	S	Cl	K	Ca	Fe
1	49.9	0.1	0.2	0.1	0.8	0.3	0.1	0	0	48.53
2	55.6	0.1	0.4	0.2	17.6	0.5	0.1	0	0	25.38
3	54.9	0.2	0.4	0.3	17.4	0.8	0.1	0	0.1	25.69
4	51.2	0	0.3	0.3	18.9	0.7	0.1	0	0.2	28.34
5	60.7	0	0.3	0.1	0.2	0.1	0	0	0.3	38.26
6	65.1	0.2	0.5	0.1	0.2	0.1	0	0	0.5	33.35
7	63.4	0.2	1.3	0.2	0.2	0.1	0.1	0	4.9	29.78
8	66.6	0.3	1.3	0.2	0.2	0	0	0	3.9	27.51
9	69.6	0.6	0.7	0.3	0.2	0	0	0	0.6	27.98
10	62.3	0	0.3	0.1	0.3	0.1	0	0	0.7	36.24
11	53.8	0.3	0.4	0.2	2.4	0.2	0.1	0	0.1	42.5

576
577
578

Table 5. Quantification of SEM-EDX analyses at the corrosion interface of the internal rod in the CIL setup. The PI are indicated in Figure 10a.

PI	Composition (at. %)										
	O	Na	Mg	Al	Si	S	Cl	K	Ca	Fe	Cu
1	58.4	0.5	0.4	0.2	0.4	0.3	0	0.0	0	39.0	0.7
2	67.0	0.7	0.5	0.2	1.0	0.9	0	0	0.1	28.9	0.7
3	56.8	0.2	0.3	0.2	17.5	0.7	0.1	0	0.1	23.9	0.2
4	54.7	0.0	0.4	0.2	14.8	0.5	0.1	0	0	29.3	0.0
5	65.8	0.7	0.5	0.2	0.4	0.8	0.1	0	0.1	30.8	0.7
6	64.9	0.3	0.7	0.1	0.3	0.2	0	0.1	5.9	27.1	0.3
7	70.6	0.4	0.5	0.1	0.1	0	0	0.1	0.4	27.2	0.4
8	72.9	0.4	1.1	0.3	0.4	0.2	0	0	6.8	17.5	0.4
9	59.5	0.8	0.6	0.3	0.9	0.6	0.5	0	0.1	35.9	0.8

579

580

581

Figures

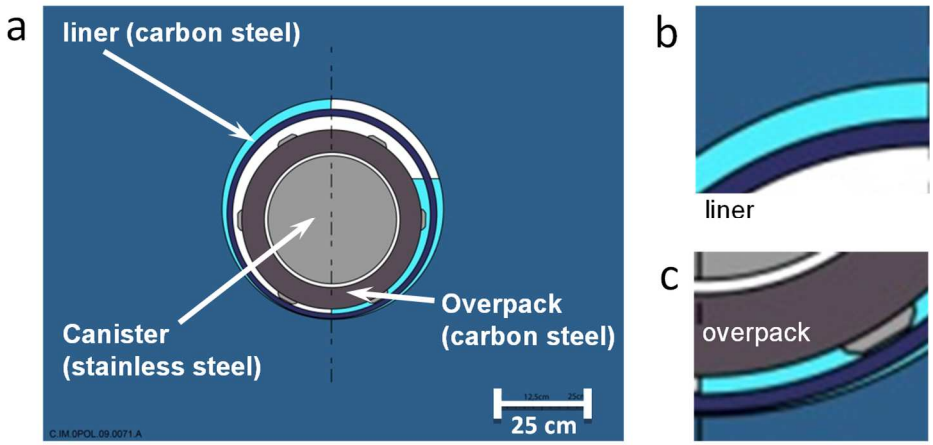

Figure 1. (a) Schematic cross-section of the former design for disposal cells in the French High-level waste repository. (b) Illustration of the gradual filling of the space between clay and the liner. (c) Illustration of the confined interspace between the liner and the overpack, resulting in corrosion under confined conditions.

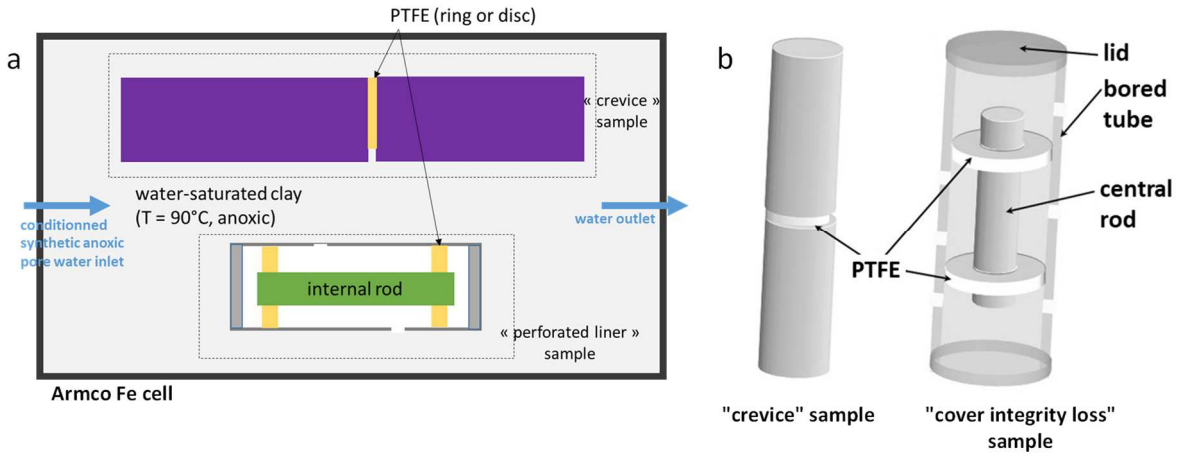

Figure 2. (a) Schematic illustration of the high-pressure cell setup and positioning of the samples. In real experiments, “crevice” and “cover integrity loss” (CIL) specimens were corroded in separate cells. (b) Illustration of the sample geometries.

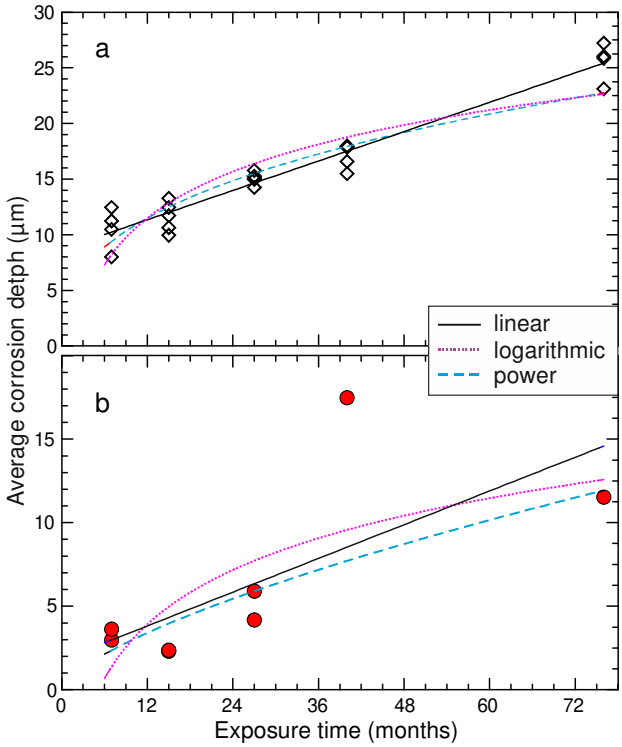

604

605

606 Figure 3. Sample damage as a function of reaction time for the massive half-rods of the simulated
607 crevices (a) and the steel rods within the CIL specimens (b). Also illustrated are the fits of
608 experimental data with logarithmic law, power law and linear law.

609

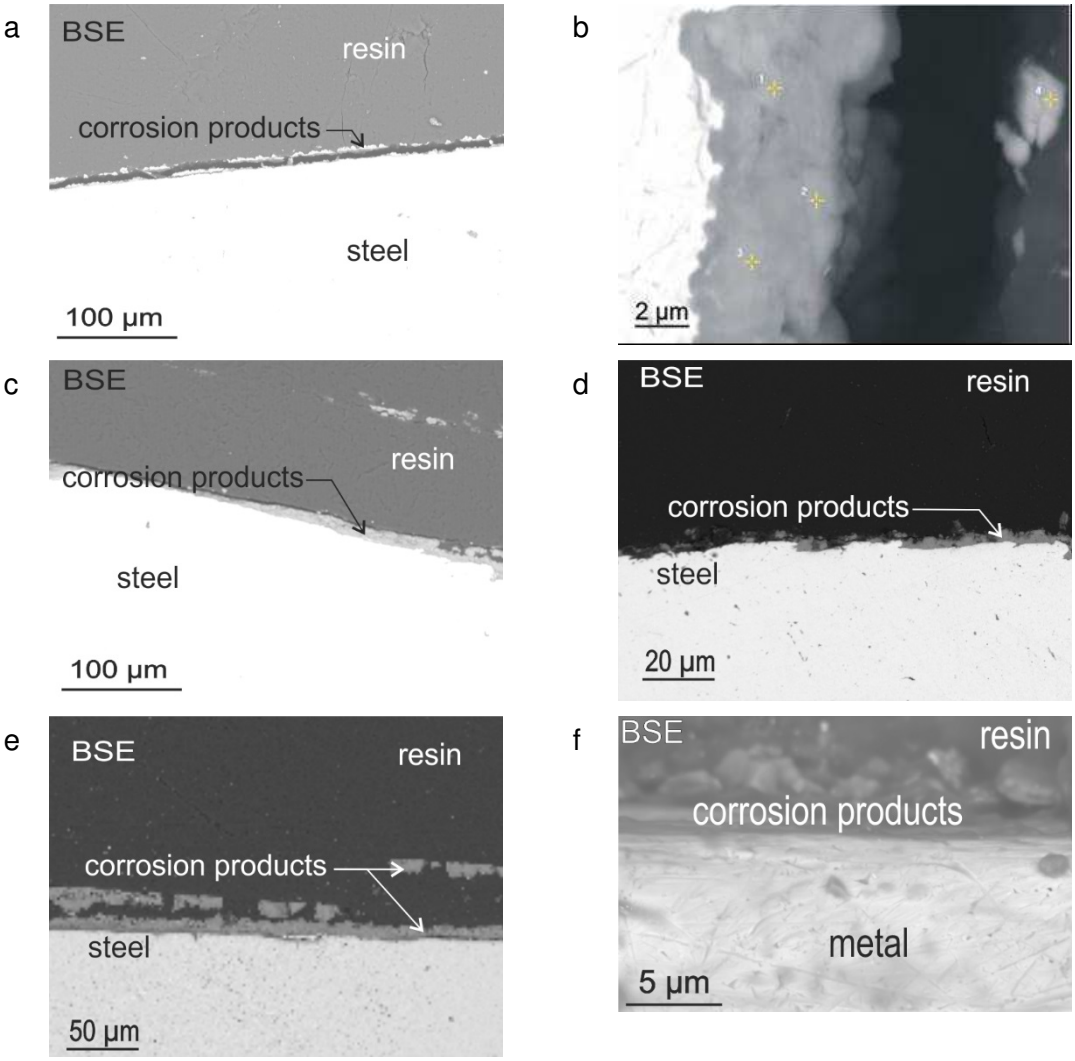

610

611 Figure 4. Scanning electron images (BSE mode) showing the evolution of the corrosion interfaces in
612 the simulated crevices as a function of reaction time. (a ,b) C07 sample, 7 months. (c) C13, 13
613 months. (d) C27, 27 months. (e) C40, 40 months. (f) C76, 76 months.

614

615

616

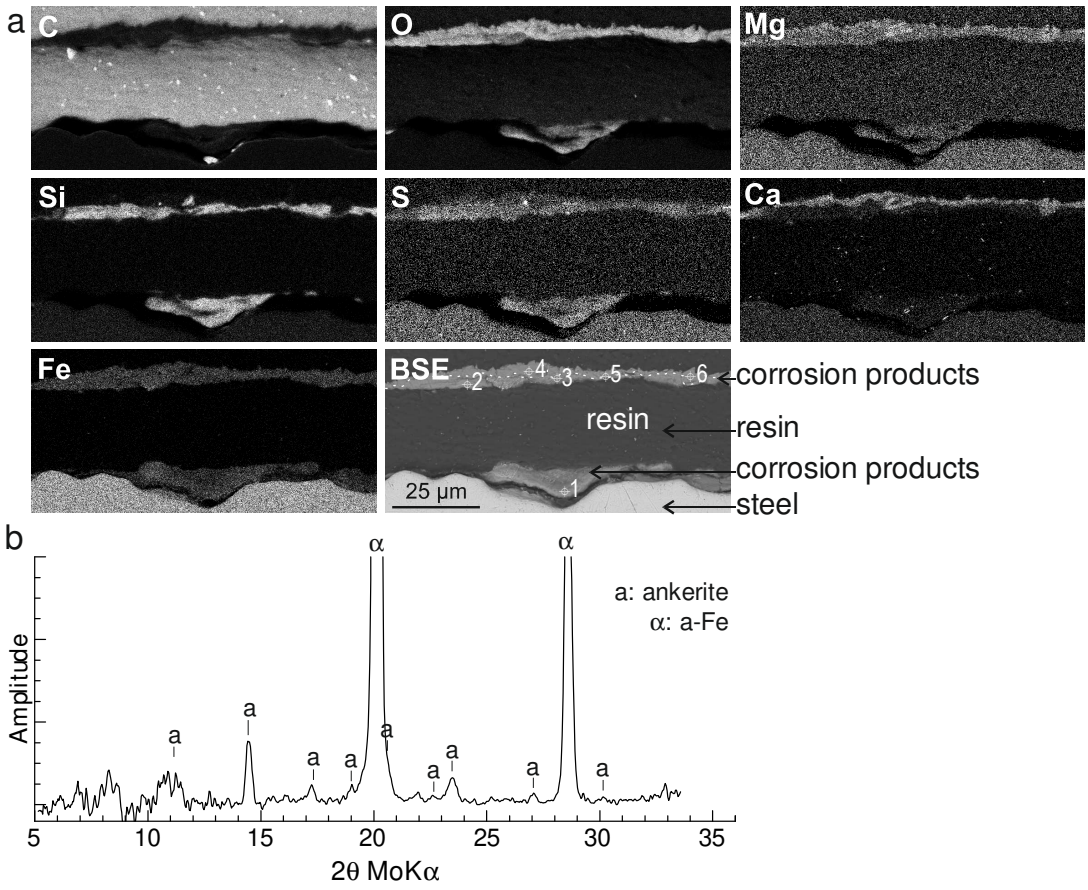

617

618

619 Figure 5. (a) Chemical mapping of element distributions at the simulated crevice interface of the C40
620 rod (40 months of reaction). The dotted line marks the interface between inner and outer
621 corrosion layers. (b) µXRD diagram of a thin slice of the simulated crevice.

622

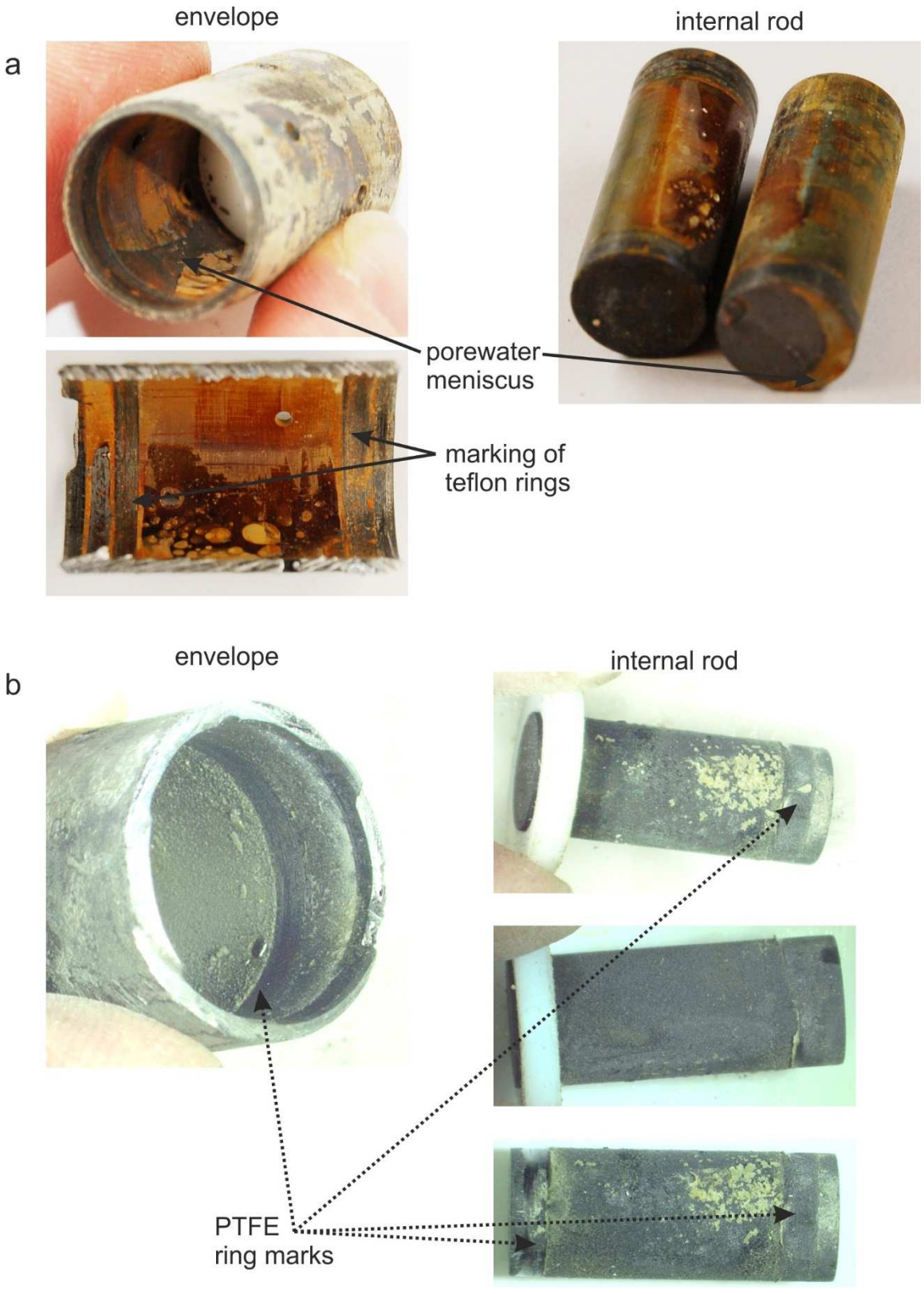

Figure 6. (a) Optical images of the two envelopes and internal rods of the CIL specimens after 15 months of reaction time, showing the presence of water marks indicating gradual filling of porewater inside the envelope. (b) Optical images of the two envelopes and internal rods of the CIL specimens after 76 months of reaction time.

629

630

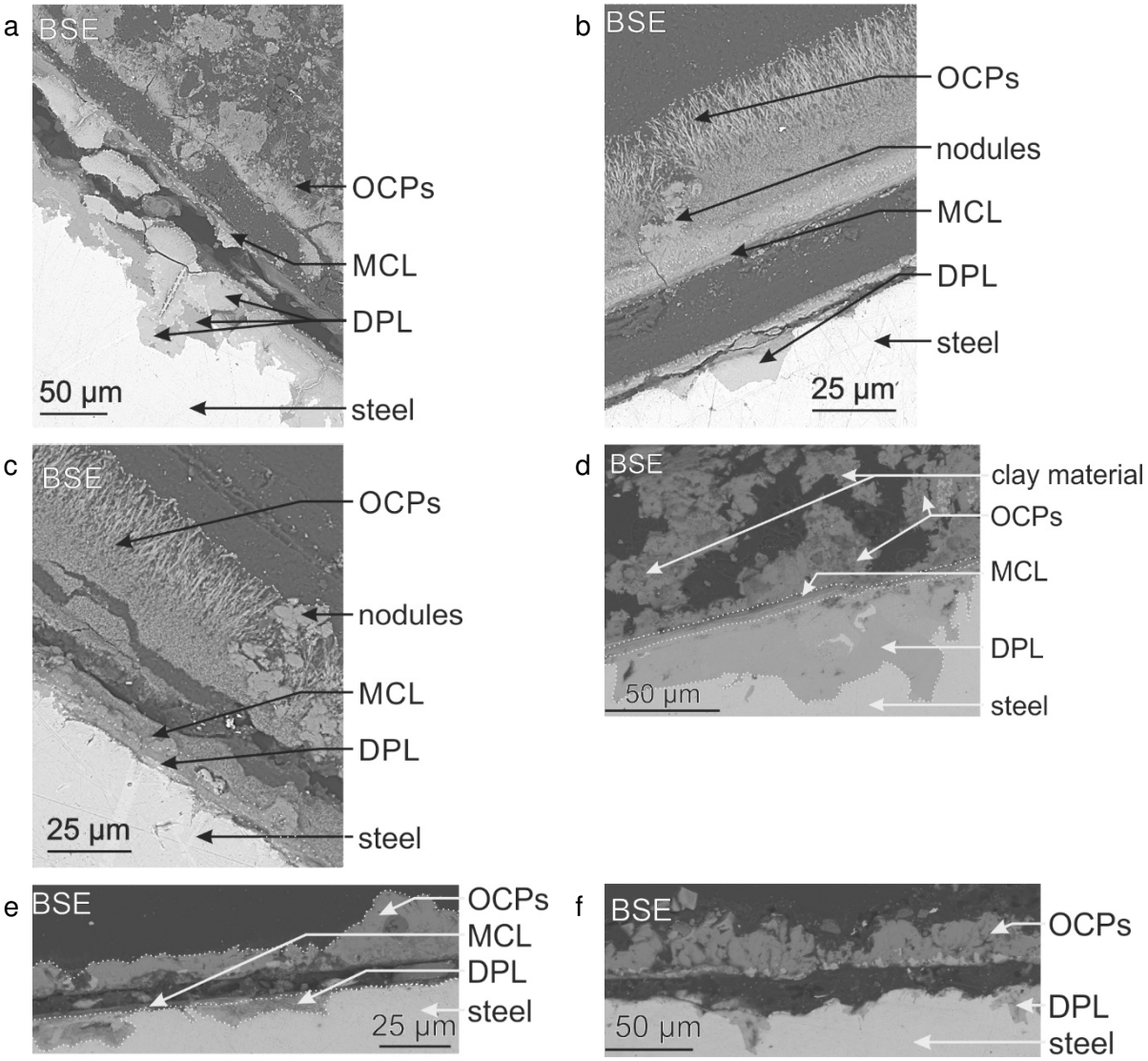

631

632 Figure 7. Scanning electron micrographs of the corrosion interfaces in the CIL setup for 40 (a-c) and
633 76 (d-f) months of reaction time. (a,d) Lower inside wall of the tube. (b,e) Central rod. (c,f) Upper
634 inside wall of the tube. DPL: dense products layer. MCL: median corrosion layer. OCPs: outer
635 corrosion products.

636

637

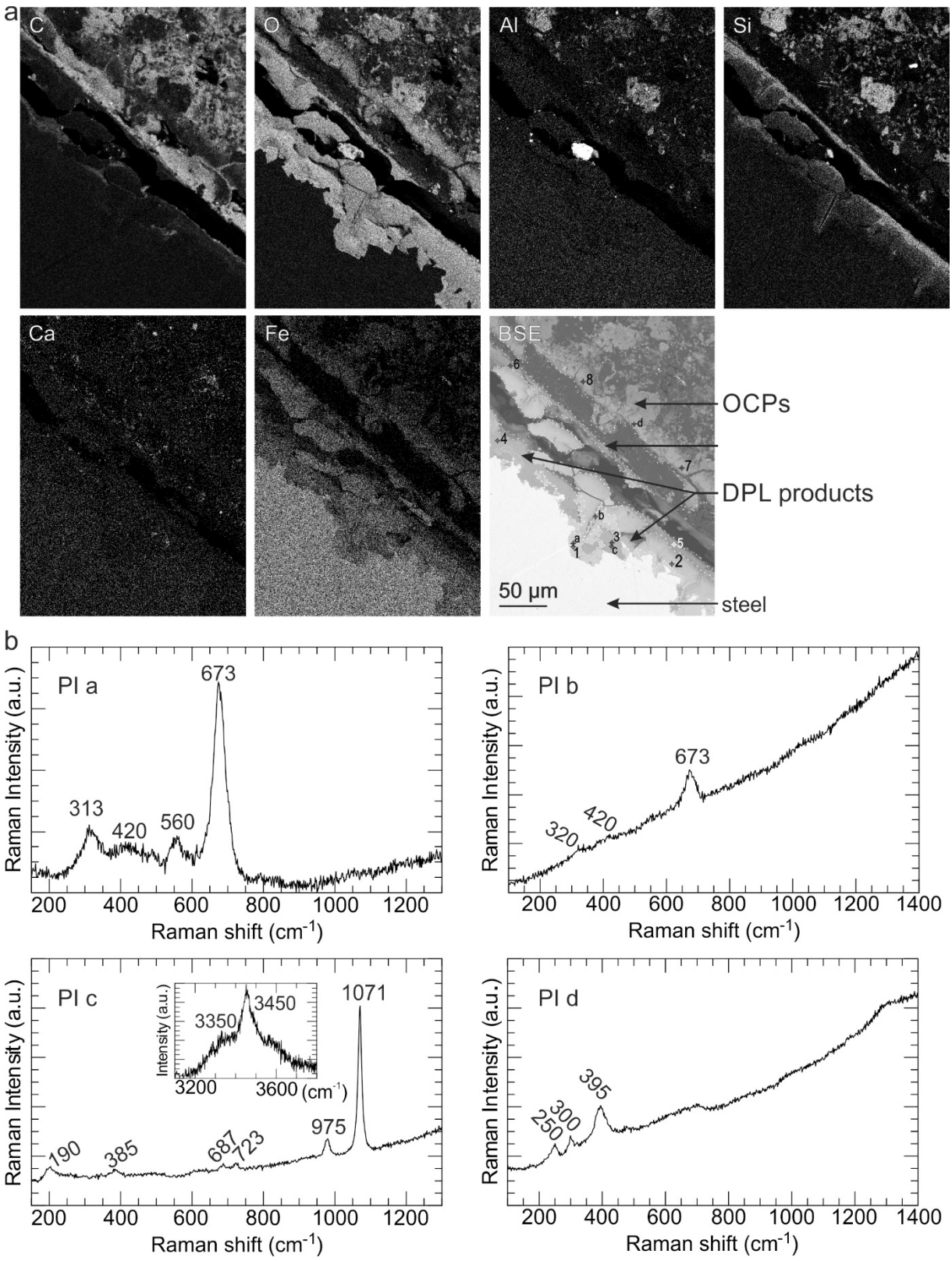

Figure 8. (a) BSE image and chemical mapping of element distributions at the lower inside wall of the CIL setup corroded for 40 months. DPL: dense products layer. MCL: median corrosion layer. OCPs: outer corrosion products. (b) µRaman spectra at selected points of interest (PI) of the corrosion interface. The PI locations are indicated on the BSE image.

644

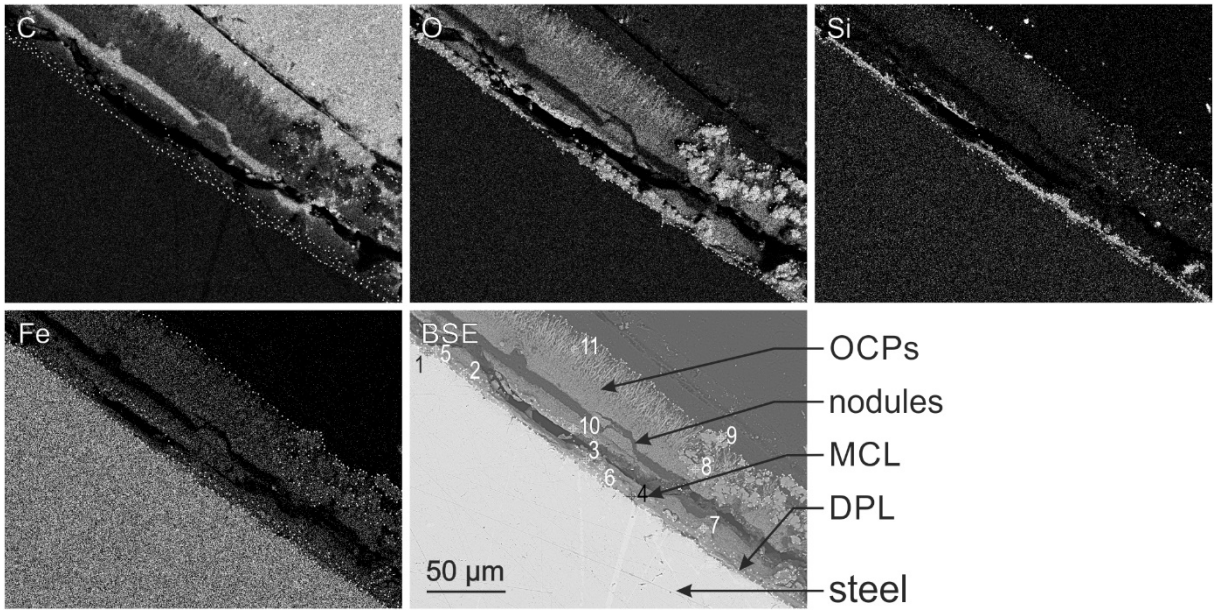

645

646 Figure 9. (a) BSE image and chemical mapping of element distributions at the upper inside wall of
647 the CIL setup corroded for 40 months.

648

649

650

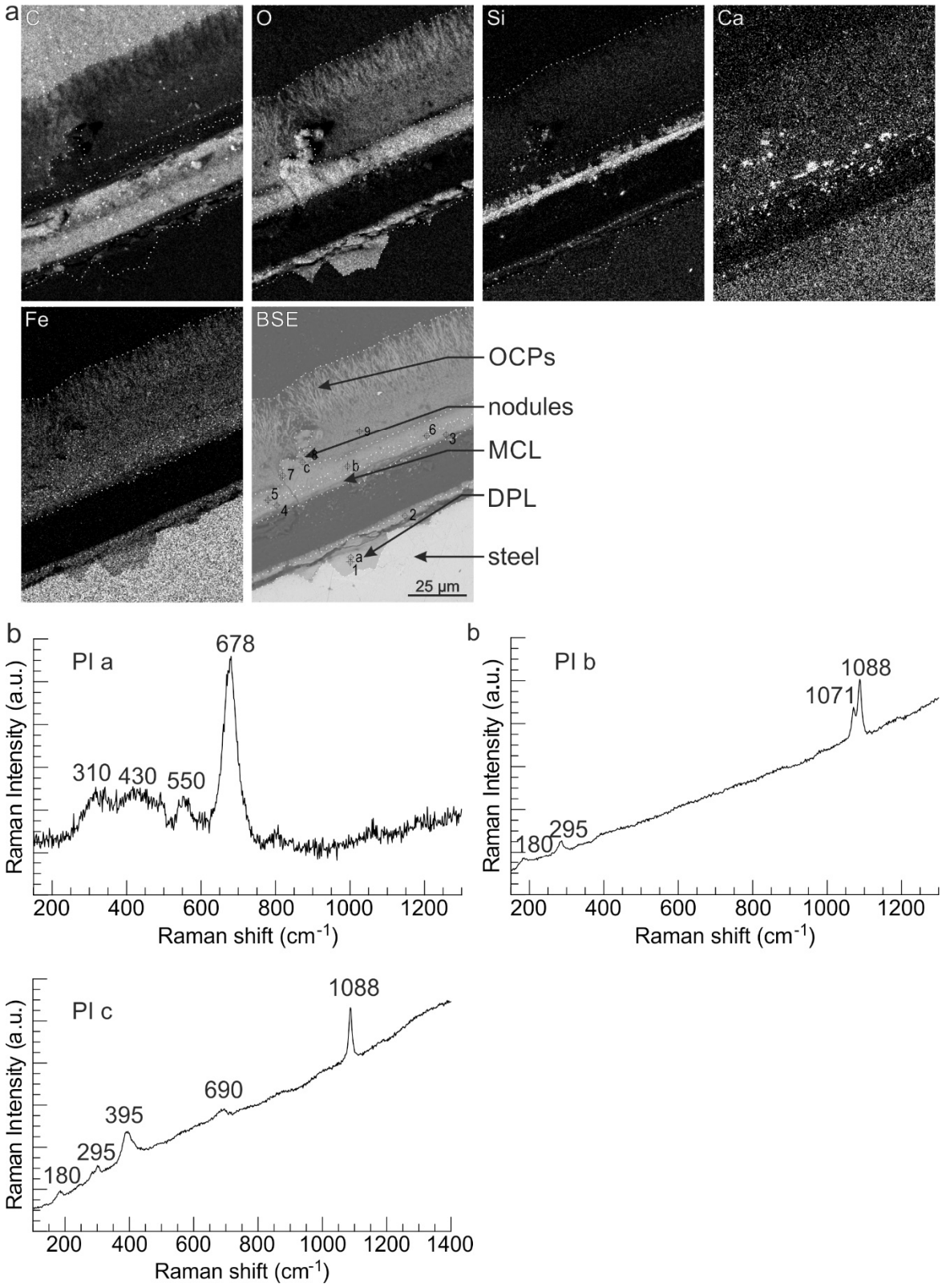

Figure 10. (a) BSE image and chemical mapping of element distributions for the corrosion interface of the central rod for the CIL setup corroded for 40 months. (b) µRaman spectra at selected points of interest (PI) of the corrosion interface. The PI locations are indicated on the BSE image.